JACS Au
AN OPEN ACCESS JOURNAL OF THE AMERICAN CHEMICAL SOCIETY

pubs.acs.org/jacsau

Article

# $VSe_{2-x}O_x$@Pd Sensor for Operando Self-Monitoring of Palladium-Catalyzed Reactions

Mingze Li,[‡] Yunjia Wei,[‡] Xingce Fan, Guoqun Li, Xiao Tang, Weiqiao Xia, Qi Hao,* and Teng Qiu*

Cite This: *JACS Au* 2023, 3, 468–475

Read Online

ACCESS | Metrics & More | Article Recommendations | Supporting Information

**ABSTRACT:** Operando monitoring of catalytic reaction kinetics plays a key role in investigating the reaction pathways and revealing the reaction mechanisms. Surface-enhanced Raman scattering (SERS) has been demonstrated as an innovative tool in tracking molecular dynamics in heterogeneous reactions. However, the SERS performance of most catalytic metals is inadequate. In this work, we propose hybridized $VSe_{2-x}O_x$@Pd sensors to track the molecular dynamics in Pd-catalyzed reactions. Benefiting from metal−support interactions (MSI), the $VSe_{2-x}O_x$@Pd realizes strong charge transfer and enriched density of states near the Fermi level, thereby strongly intensifying the photoinduced charge transfer (PICT) to the adsorbed molecules and consequently enhancing the SERS signals. The excellent SERS performance of the $VSe_{2-x}O_x$@Pd offers the possibility for self-monitoring the Pd-catalyzed reaction. Taking the Suzuki−Miyaura coupling reaction as an example, operando investigations of Pd-catalyzed reactions were demonstrated on the $VSe_{2-x}O_x$@Pd, and the contributions from PICT resonance were illustrated by wavelength-dependent studies. Our work demonstrates the feasibility of improved SERS performance of catalytic metals by modulating the MSI and offers a valid means to investigate the mechanisms of Pd-catalyzed reactions based on $VSe_{2-x}O_x$@Pd sensors.

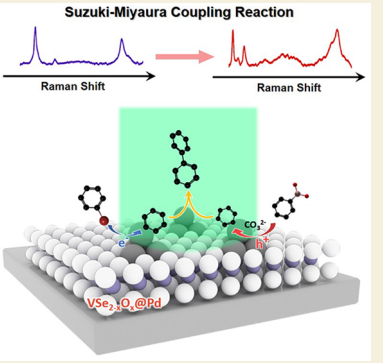


**KEYWORDS:** *two-dimensional materials, vanadium selenide, metal−support interaction, palladium catalysts, Suzuki−Miyaura coupling reaction, photoinduced charge transfer, surface-enhanced Raman spectroscopy*

## INTRODUCTION

Palladium (Pd) has become a cornerstone of synthetic chemistry by virtue of its excellent stability and superior surface catalytic activity.[1] The Pd-catalyzed coupling reactions have been widely applied in the fabrication of organic molecular frameworks, including the synthesis of aniline, substituted alkene, and functional group-containing olefins as well as styrene and biphenyl.[2−4] Nevertheless, the dynamics of theses complicated reactions are not always clear because of a lack of experimental techniques in clarifying the molecular evolutions at the palladium interface.

Surface-enhanced Raman scattering (SERS), which features single-molecule sensitivity and chemically specific identification, has been demonstrated as an innovative tool in tracking the molecular dynamics in heterogeneous reactions.[5] It generally employs metallic plasmonic structures to generate localized surface plasmon resonance (LSPR) to boost the Raman scattering of the target molecule with an enhancement factor up to $10^8$−$10^{10}$.[6,7] This strategy, which is known as the electromagnetic (EM) enhancement, has been successfully applied in investigating palladium-catalyzed reactions by constructing plasmonic core−shell or core−satellite composites.[8,9] However, the LSPR-based SERS strategy is accompanied by the plasmon-induced hot carriers and thermal effects.[10] To be specific, the plasmon would decay into energetic hot carriers within the metal via Landau damping and then transfer the energy to the surrounding environment and cause significant thermal effects near the metal surface.[11,12] These additional factors may cast a shadow on the validity of the findings of the Pd-catalyzed coupling reactions.

Considering the difficulties in addressing the above intrinsic limitations of EM, it is of great importance to circumvent these obstacles to realize self-monitoring of Pd-catalyzed reactions.[13] Photoinduced charge transfer (PICT) processes between the Pd catalyst and molecules could magnify the Raman scattering cross section of the molecule−Pd catalyst system (also called the chemical mechanism, CM), which is the key for plasmon-free SERS enhancement.[14−17] However, the enhancement factor of the PICT-based strategy is originally weak. Although heterojunction engineering,[18−22] defect engineering,[23−26] and many other surface techniques have been proposed to improve the sensitivity of CM-based strategy,[27−29] it is hard to improve the PICT between the Pd catalyst and molecules. As reported in the literature, metal−support interactions (MSI), including the orbital rehybridizations and charge transfer across the

Received: November 1, 2022
Revised: December 31, 2022
Accepted: January 3, 2023
Published: January 16, 2023

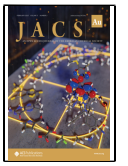

metal−support interface, would profoundly affect the properties of the catalysts. Modulating MSI by selecting suitable support has been considered as an effective approach to modulate the electronic structure of supported metal catalysts.[30,31] We suggest that rational structural design of catalysts based on MSI may improve the PICT between Pd catalyst and molecules, enabling the Pd-support system to track the SERS dynamics in Pd-catalyzed reactions.

In this work, we propose two-dimensional Pd hybridized defective $VSe_2$ ($VSe_{2-x}O_x$@Pd) sensors to realize self-monitoring of Pd-catalyzed reactions based on operando SERS strategy. The significantly improved SERS performance of $VSe_{2-x}O_x$@Pd is attributed to the electronic structure modulation of atomic-level Pd clusters due to MSI. For one thing, the surface defects of selenium provide favorable sites for the doping of oxygen and assembly of Pd clusters, authorizing energetic charge exchanges between the Pd and $VSe_{2-x}O_x$ nanosheets. For another, the combination of the Pd clusters and metallic phase $VSe_{2-x}O_x$ nanosheets further enriches the density of states (DOS) at the Fermi level of the hybrid system, and improves the probability of charge transfer between the hybrid system and adsorbed molecules.[32,33] These advantages endow $VSe_{2-x}O_x$@Pd sensors the ability to visualize the Pd-catalyzed coupling reactions in a valid manner.

## RESULTS AND DISCUSSION

Efficient assembly of the Pd catalyst on $VSe_2$ nanosheets is the prerequisite to fabricate the $VSe_{2-x}O_x$@Pd sensor. Layered $VSe_2$ is bound by a van der Waals force, and its crystal structure is depicted in Figure 1a. Manufacturing Se defects on exfoliated $VSe_2$ is conducive to the selectively assembly of Pd clusters (detailed experimental methods are shown in Figure S1), and the schematic illustration is shown in Figure 1b. As for the pristine $VSe_2$ nanosheet, it was characterized by high-resolution transmission electron microscopy (TEM) in Figure 1c. The fast Fourier transform (FFT) pattern in the inset suggests a 6-fold rotational symmetric diffraction, which is consistent with the lattice structure of the hexagonal $VSe_2$ crystal in Figure 1a.[34] The flat surface of exfoliated $VSe_2$ nanosheets is displayed in Figure 1d by scanning electron microscopy (SEM) using Si substrate as a contrast, and the thickness of the thinnest exfoliated $VSe_2$ nanosheet was estimated to be ∼3.2 nm by atomic force microscopy (AFM) in Figure 1e.

Furthermore, more experimental evidence was provided to demonstrate the assembly of Pd clusters on $VSe_2$. First, X-ray photoelectron spectroscopy (XPS) was conducted to verify the chemical state and composition of the $VSe_{2-x}O_x$@Pd sample. As Figure 1f shows, the appearance of Pd 3d peaks proved the existence of the Pd element on $VSe_{2-x}O_x$@Pd, and the binding energy of Pd $3d_{5/2}$ of $VSe_{2-x}O_x$@Pd is about 336 eV, which is between the metallic Pd (335 eV) and Pd−O (336.5 eV), suggesting that the Pd clusters were positively charged overall.[35,36] Meanwhile, the broadened Se 3d peak at 54.6 eV of $VSe_{2-x}O_x$@Pd arises from the superposition of the peaks of Pd 4p and Se−O bond.[37] The broadened V $2p_{3/2}$ and V $2p_{1/2}$ peaks at ∼513.6 and ∼521.2 eV of $VSe_{2-x}O_x$@Pd originate from the $V^{5+}$ component induced by oxygen doping.[32,38] Raman characterizations also demonstrate that the oxygen doping had been introduced to the sample (Figures S2). In addition, the X-ray diffraction (XRD) of the pristine $VSe_2$ and $VSe_{2-x}O_x$@Pd sensors are compared in Figure 1g. The XRD shows that the peaks of the $VSe_2$ were unchanged after Pd loading, indicating that the lattice of $VSe_{2-x}O_x$ is not severely damaged during the treatment.[39] Specifically, the diffraction peaks corresponding to the metallic Pd crystal are not observed, indicating that the Pd clusters were dispersed on $VSe_{2-x}O_x$ and no bulk formed.[40]

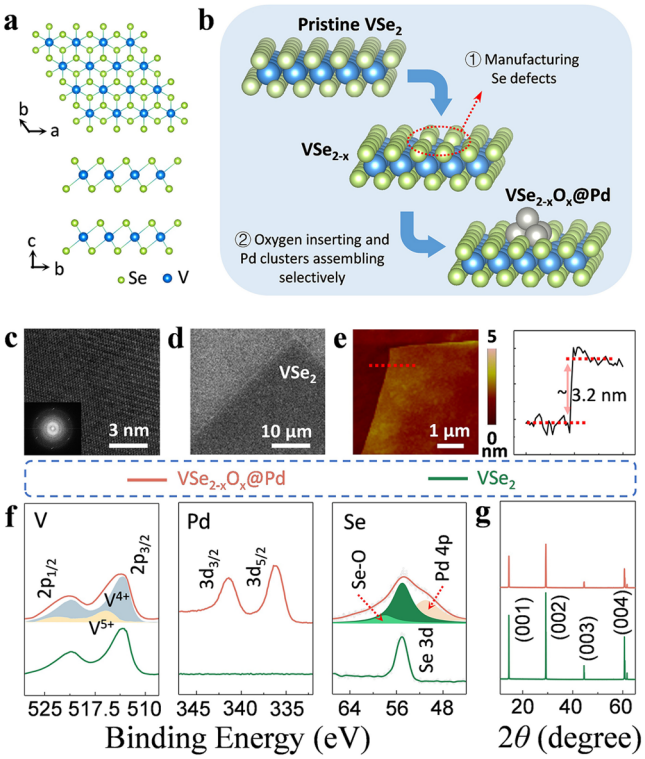


**Figure 1.** Preparation and characterization of the samples. (a) Top and side views of the atomic structure of the layered $VSe_2$ crystal. (b) Schematic illustration of the fabrication mechanism of the $VSe_{2-x}O_x$@Pd sensor. (c) High-resolution TEM image of ultrathin $VSe_2$ nanosheets. Inset: corresponding FFT image. (d) SEM, (e) AFM topography image and the corresponding height profile of the ultrathin $VSe_2$ nanosheets. (f) High-resolution XPS of Se 3d, Pd 3d and V 2p spectra of the $VSe_2$ nanosheets and $VSe_{2-x}O_x$@Pd, respectively. (g) XRD of the $VSe_2$ nanosheets and $VSe_{2-x}O_x$@Pd sensor.

To further reveal the microtopography of the $VSe_{2-x}O_x$@Pd surface, the energy-dispersive spectroscopy (EDS) elemental analyses combined with TEM and high angle annular dark-field (HAADF) were conducted to exhibit the elemental distribution on $VSe_{2-x}O_x$@Pd in Figure 2a−c. As for the prepared $VSe_{2-x}O_x$@Pd sensor, the Pd element was densely distributed on the surface. The weights of different elements of the entire sample are supplemented in Figure S3. Moreover, the high-resolution TEM in Figure 2d reveals that the atomic-level Pd clusters, marked by red boxes, were loaded at the oxygen-doping selenium defects on the $VSe_2$ surface (large area TEM image see Figure S4), resulting in the rougher surface of $VSe_{2-x}O_x$@Pd (Figure S5). The typical nanostructure of $VSe_{2-x}O_x$@Pd was emphasized in Figure 2d and selected to be simulated for subsequent calculations.

The selectively assembly of Pd cluster on oxygen-doping selenium defects is important to the formation of $VSe_{2-x}O_x$@Pd. The role of oxygen-doping selenium defects can be demonstrated by density-functional theory (DFT) calculations, as shown in Figure 3a. The DFT results show that the energy barrier ($E_b$) for the dechlorination of $[PdCl_4]^{2-}$ ion on the


https://doi.org/10.1021/jacsau.2c00596
JACS Au 2023, 3, 468−475

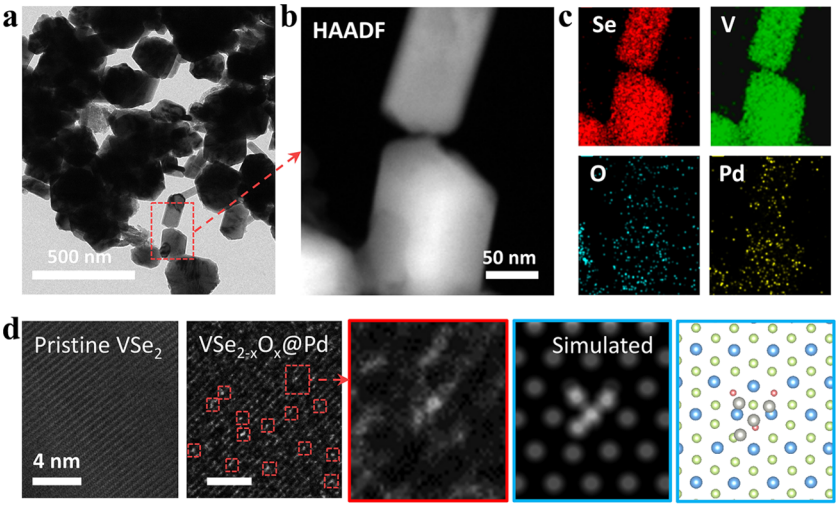


**Figure 2.** (a) TEM image, (b) HAADF image, and (c) corresponding elemental mappings of the as-prepared $VSe_{2-x}O_x$@Pd nanosheets. (d) From left to right: High-resolution TEM images of the $VSe_{2-x}O_x$@Pd sensor with different magnifications, schematic diagrams of the zoomed TEM image and corresponding simulated atomic arrangements of $VSe_{2-x}O_x$@Pd, respectively. The dispersed bright dots in the red boxes are the Pd clusters loaded on $VSe_{2-x}O_x$.

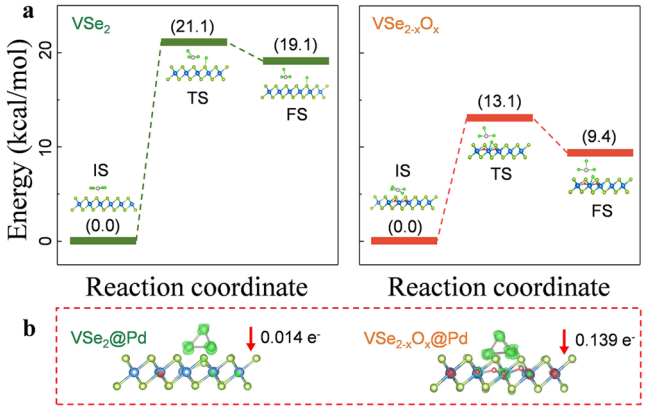


**Figure 3.** Formation of Pd cluster on $VSe_2$ and $VSe_{2-x}O_x$: the oxygen-doping Se defects matter. (a) The minimum energy pathways, including the initial state (IS), transition state (TS) and final state (FS), for dichlorination of the $[PdCl_4]^{2-}$ ion on $VSe_2$ and $VSe_{2-x}O_x$ surface, respectively. (b) The charge exchange in typical nanostructure of $VSe_2$@Pd and $VSe_{2-x}O_x$@Pd. The red and green colors represent the region of the increased electron density and decreased electron density, respectively.

$VSe_{2-x}O_x$ surface is only 13.1 kcal/mol, whereas $E_b$ reaches 21.1 kcal/mol on the $VSe_2$ surface. The results show that the $VSe_{2-x}O_x$ provides more favorable sites for the reduction of $[PdCl_4]^{2-}$ at room temperature. Meanwhile, as shown in Figure 3b, after the assembly of Pd clusters on the pristine $VSe_2$ ($VSe_2$@Pd) or $VSe_{2-x}O_x$ surface, the charge exchange between the Pd cluster and $VSe_{2-x}O_x$ of $VSe_{2-x}O_x$@Pd (0.139 e/molecule) is an order of magnitude higher than that of $VSe_2$@Pd (0.014 e/molecule). The strong charge exchange in $VSe_{2-x}O_x$@Pd leads to positively charged Pd clusters, which is consistent with the XPS data in Figure 1f. All results demonstrate that the presence of oxygen-doping selenium defects facilitates the formation of Pd clusters and charge exchange between Pd clusters and $VSe_{2-x}O_x$, which may favor molecule−$VSe_{2-x}O_x$@Pd interactions.

To investigate the SERS performance of the $VSe_{2-x}O_x$@Pd sensor, 4-bromothiophenol (BTP) and rhodamine 6G (R6G) were employed as Raman probes for SERS studies under 532 and 633 nm lasers, respectively. Additionally, to further clarify the commendable SERS performance of $VSe_{2-x}O_x$@Pd sensor, $VSe_2$@Pd, pristine $VSe_2$, and graphene (typical metallic two-dimensional material) were taken as comparisons. As shown in Figure 4a, the fingerprint signals of BTP (C−Br vibrational mode at 1065 $cm^{-1}$ and C−C vibrational mode of benzene ring at 1560 $cm^{-1}$) are clearly discerned from the $VSe_{2-x}O_x$@Pd sensor, whereas they are fairly weak from the other substrates.[41,42] Like BTP, the strongest SERS signals of R6G were observed from the $VSe_{2-x}O_x$@Pd sensor in controlled experiments (Figure 4b). The SERS signals from the $VSe_{2-x}O_x$@Pd samples of different batches are highly reproducible with a relative standard deviation of ∼9.11% (Figure S6). The enhancement factor of $VSe_{2-x}O_x$@Pd for $10^{-3}$ M BTP is calculated to be about $1.04\times 10^3$ (Figure S7). Considering that the plasmonic effects of the planar $VSe_{2-x}O_x$@Pd are negligible under our experimental conditions because the plasmonic adsorption of $VSe_2$ is located at the infrared band and the plasmonic resonance effect of highly dispersed Pd clusters is also negligible,[43] we can deduce that the CM enhancement is the dominating factor for SERS. As shown in Figure 4c, the SERS signals of molecules on the $VSe_{2-x}O_x$@Pd showed a strong dependence on the laser energy. Strong SERS signals of R6G were observed at 532 nm and no signal was discerned at 633 nm, whereas stronger SERS was obtained at 633 nm for BTP and a weakened signal turned up at 532 nm. This selective enhancement, which differs in CM enhancement compared the conventional EM enhancement, is determined by the coupling between the laser wavelength and molecular energy bands and can be considered as strong evidence to demonstrate that CM is the dominating mechanism for the $VSe_{2-x}O_x$@Pd SERS sensor.[44]

To reveal the underlying SERS mechanism of the $VSe_{2-x}O_x$@Pd sensor, corresponding first-principles calculations based on density functional theory were conducted. According to the CM mechanisms, the PICT in analytes-$VSe_{2-x}O_x$@Pd system would be significantly related to the band structure of $VSe_{2-x}O_x$@Pd. The hybrid band structure of $VSe_{2-x}O_x$@Pd originated from the combined contribution of


https://doi.org/10.1021/jacsau.2c00596
JACS Au 2023, 3, 468−475

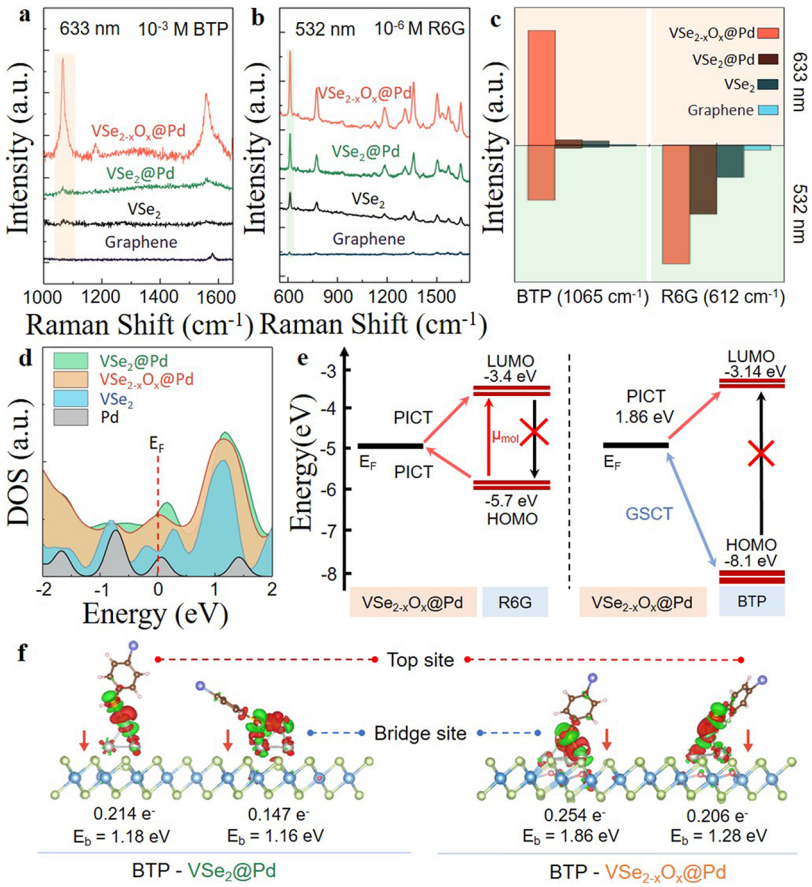


**Figure 4.** Performance and mechanisms of the $VSe_{2-x}O_x$@Pd sensor. SERS spectra of (a) $10^{-6}$ M R6G and (b) $10^{-3}$ M BTP from $VSe_{2-x}O_x$@Pd sensor, $VSe_2$@Pd, pristine $VSe_2$ nanosheets, and graphene. (c) Integrated Raman intensity of $10^{-3}$ M BTP and $10^{-6}$ M R6G on different substrates under 532 or 633 nm laser. (d) DOS near the Fermi energy of Pd cluster, $VSe_2$, $VSe_2$@Pd, and $VSe_{2-x}O_x$@Pd. (e) Schematic diagram of the PICT between the $VSe_{2-x}O_x$@Pd sensor and R6G or BTP under excitation. The black arrows indicate the inhibited charge transfer pathways. (f) Calculated binding energy and corresponding side views of the electron density difference isosurface (0.002 electron/bohr$^3$) of different adsorption sites of BTP on $VSe_{2-x}O_x$@Pd and $VSe_2$@Pd, respectively. The red and green colors represent the region of the increased electron density and decreased electron density, respectively.

the Pd cluster and $VSe_2$ (Figure S8). Compared with the band structure of pristine $VSe_2$ and Pd cluster, the density of state (DOS) near the Fermi level of $VSe_{2-x}O_x$@Pd is more abundant (Figure 4d). According to Fermi's golden rule, the large number of allowed energy states would be beneficial to the charge transition.[45−47] As illustrated in Figure 4e, the higher DOS at the Fermi level promotes the PICT between the $VSe_{2-x}O_x$@Pd and molecular energy levels under excitation, resulting in a significant enhancement for Raman scattering.

Besides, the positively charged Pd offers stronger adsorption sites for the negatively charged groups, and thus improved PICT can be expected. Taking the BTP molecule as an example, we studied the adsorption of BTP on $VSe_{2-x}O_x$@Pd and $VSe_2$@Pd surfaces with two main adsorption sites (top-site and bridge-site, see Figure S9). The results in Figure 4f show that the binding energies of BTP-$VSe_{2-x}O_x$@Pd and BTP-$VSe_2$@Pd were 1.86 and 1.16 eV, respectively, for the bridge-site and 1.28 and 1.18 eV, respectively, for the top-site. The binding energy of the bridge-adsorbed BTP-$VSe_{2-x}O_x$@Pd was ∼70% higher than that of the BTP-$VSe_2$@Pd, suggesting a significantly stronger coupling between the BTP and $VSe_{2-x}O_x$@Pd. Moreover, the electron density difference isosurfaces (0.002 electron/bohr$^3$) of the above complexes exhibit the electron perturbation that arises from the charge transfer from BTP to the substrates, suggesting the formation of an interface dipole. Benefiting from the strong charge exchange between Pd clusters and $VSe_{2-x}O_x$, the strongest electron transfer (0.254 e/molecule) occurred between BTP and $VSe_{2-x}O_x$@Pd at the bridge-site, indicating a more pronounced ground-state charge transfer (GSCT). Both of these effects strengthen the molecular adsorption on Pd clusters, which is beneficial for the CM-based SERS enhancement.

The excellent SERS performance of the $VSe_{2-x}O_x$@Pd sensor provides the possibility to realize self-monitoring of Pd-catalyzed reaction. The Suzuki−Miyaura coupling reaction (SM reaction) is a category of palladium-catalyzed cross-coupling reactions between aryl (or alkenyl) boronic acid (or boronic acid esters) and halogenated aromatics (or alkenes).[48−50] In this part, we adopt a Pd-catalyzed coupling between BTP and phenylboronic acid (BPA) to form 4-mercaptobiphenyl (MBP) in an alkaline liquid-phase environment as a model SM reaction for investigation (Figure 5a). The reaction processes of the SM reaction on $VSe_{2-x}O_x$@Pd are divided into three steps. On the one hand, the C−X (X = Cl, Br, I) bond of the halogenated arene adsorbed on Pd clusters in the $VSe_{2-x}O_x$@Pd system would break under photoexcitation. This step is the rate-determining step, in which the electrons are transferred from Pd clusters to C and Br atoms to form C−Pd and Br−Pd bonds. On the other hand,


https://doi.org/10.1021/jacsau.2c00596
JACS Au 2023, 3, 468−475

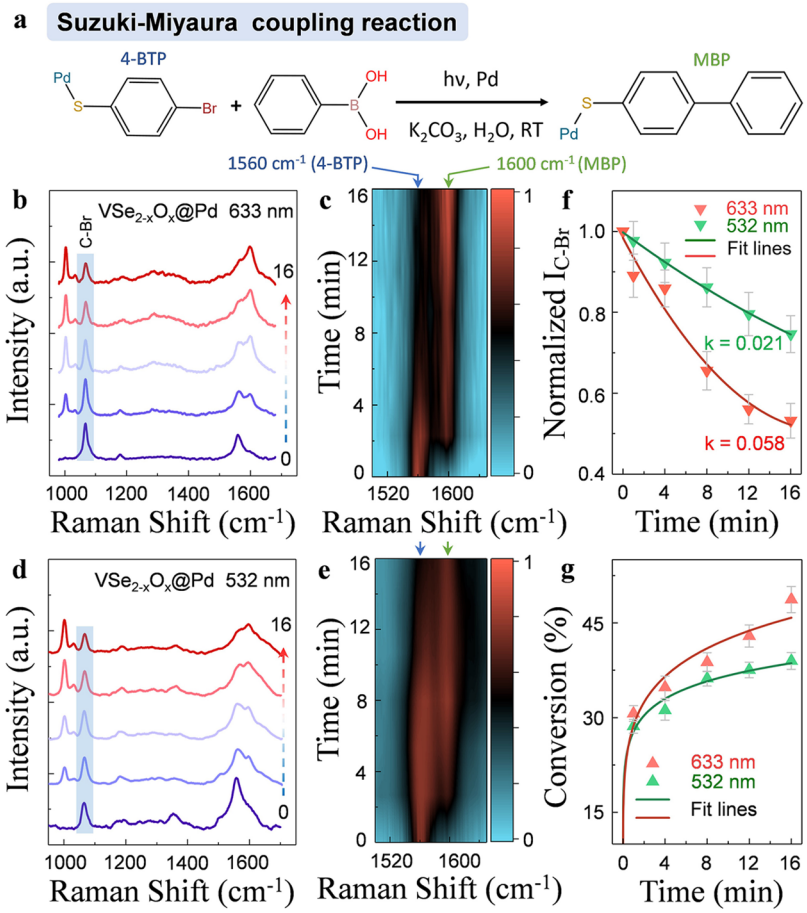


**Figure 5.** SERS investigations of the SM reaction on $VSe_{2-x}O_x$@Pd. (a) Schematic diagram of the SM reaction. (b–e) Typical time-dependent SERS spectra of the SM reaction on the $VSe_{2-x}O_x$@Pd sensor and corresponding Raman contour plots under 633 nm (b, c) and 532 nm laser (d, e), respectively. (f) Normalized breakage rates of the C–Br bond fitted with second order kinetics and (g) time-dependent conversion rates of BTP on $VSe_{2-x}O_x$@Pd under different lasers.

phenylboronic acid would be converted to borate anion with the assistance of $CO_3^{2-}$ and subsequently combines with the hole in $VSe_{2-x}O_x$@Pd to activate the C–B bond. The organic species in the above two processes would couple to form the final biphenyl product.[51] Figure 5b presents the typical SERS spectra of the SM reaction on the $VSe_{2-x}O_x$@Pd under 633 nm laser irradiation for 16 min. The distinctive new modes at 1600 $cm^{-1}$ were observed during the reactions. The SERS spectra at the wavenumber ranging from 1500 to 1670 $cm^{-1}$ were extracted and replotted in Figure 5c. It can be found that the peak at 1560 $cm^{-1}$ (BTP) weakened as the reaction proceeded while the peaks at 1600 $cm^{-1}$ (MBP) intensified. There is no peak of byproduct 4,4′-biphenyldithiol observed (details available in section IV of the Supporting Information, Figures S10–S17).[52−55] For comparison, the typical SERS spectra and contour plots employing the $VSe_{2-x}O_x$@Pd sensor under 532 nm laser are displayed in Figure 5d,e. According to the PICT resonance theory, the charge transfer between the $VSe_{2-x}O_x$@Pd and BTP would be efficiently promoted when the laser energy ($E_{633}$ = 1.96 eV) is closed to the energy gap between the Fermi level of the Pd cluster and the LUMO level of BTP (~1.86 eV) (details available in section V of the Supporting Information, Figures S18 and S19). The results show that the SM reaction can still proceed but the breakage rate of the C–Br bond at 1065 $cm^{-1}$ is obviously slower under a nonresonant 532 nm laser (Figure 5f). The C–Br bond breaking reaction follows the second-order kinetics under both 633 and 532 nm lasers (Figure S20), and the reaction constant is $k_{633}$ ~ 0.058 and $k_{532}$ ~ 0.021, respectively. The time-dependent conversion rates of BTP under different lasers were depicted in Figure 5g. By comparing the conversion rates of BTP on $VSe_{2-x}O_x$@Pd under different lasers, the contribution of the PICT resonance effect in the catalytic process can be clearly evaluated, which is difficult to study using conventional LSPR-based sensors.

## CONCLUSION

In summary, we performed operando SERS monitoring of the Pd-catalyzed SM reaction with the $VSe_{2-x}O_x$@Pd sensors. The oxygen-doped selenium defects provide efficient adsorption sites for the Pd clusters and facilitate the charge exchanges between the Pd clusters and $VSe_{2-x}O_x$. Meanwhile, the combination of Pd and $VSe_{2-x}O_x$ significantly increases DOS near the Fermi level of $VSe_{2-x}O_x$@Pd. These MSI between Pd and $VSe_{2-x}O_x$ significantly promote the PICT between the Pd clusters and adsorbed molecules, leading to intense CM enhancement which is in favor of the operando SERS monitoring of the SM reactions on Pd clusters. We observed the wavelength dependence of the SM reactions on the $VSe_{2-x}O_x$@Pd sensor and explored the contributions from PICT resonance to the catalytic conversion rate. This work demonstrates the feasibility of the $VSe_{2-x}O_x$@Pd for self-


https://doi.org/10.1021/jacsau.2c00596
JACS Au 2023, 3, 468–475

monitoring of Pd-catalyzed reactions and offers a valid MSI-based approach to investigate the reaction mechanisms.

## EXPERIMENTAL METHODS

### Sample Preparation

Single-crystal $VSe_2$ was prepared by the chemical vapor transport method using 5% excess selenium as the transporting agent. High-purity V and Se powder elements were mixed and sealed in a silica ampule. The $VSe_2$ nanosheets were obtained by a mechanical exfoliation method. The exfoliated $VSe_2$ nanosheets were annealed in vacuum at 350 °C for 30 min and subsequently immersed in 10 mL of $Na_2PdCl_4$ aqueous solution ($10^{-3}$ mol/L) for 20 min to fabricate the $VSe_{2-x}O_x$@Pd sensor. The $VSe_2$@Pd samples were produced by reducing and assembling Pd clusters onto the pristine $VSe_2$ nanosheets and naturally drying.

The Au NPs were fabricated by employing ultrathin anodic aluminum oxide membranes as templates in thermal evaporation. The prepared Au NPs were transferred in the reaction vessel where 4 mL of deionized water, 0.3 mL of $Na_2PdCl_4$ solution (2.4 mM), 2 μL of HCl solution (6 M), and 1 mL of ascorbic acid solution (100 mM) were mixed under vigorous stirring at 80 °C for 3 h to fabricated the Au@Pd NPs.

### Raman Measurements

R6G (99%, Sigma-Aldrich) and BTP (97%, Sigma-Aldrich) were employed as SERS probes. The samples were immersed in 10 mL of solution containing SERS probes for 10 min for molecule adsorption and naturally dried in the air. The Raman measurements were performed with a HORIBA Jobin Yvon Lab RAM HR 800 micro-Raman spectrometer system with a laser spot of ∼1 $\mu m^2$. The excitation wavelength was 532 or 633 nm, and the laser power was ∼2 mW unless specified. The Raman spectra were obtained with 10 s acquisition time unless specified. For the SERS measurements at the liquid state, we collected the signals from substrates in a self-designed reaction cell filled with reaction solution. The spectra for comparison were obtained under identical measurement conditions and normalized by an internal standard method.

### Density Functional Theory (DFT) Calculations

First-principles calculations were performed by using the plane-wave technique as implemented in the Vienna Ab Initio simulation package (VASP). The ion−electron interaction was described by the projector augmented wave (PAW) method, and the generalized gradient approximation (GGA) was expressed by the functional of Perdew, Burke, and Ernzerhof (PBE). The Brillouin zone integration was sampled by the gamma only method. The systems were simulated with a periodic boundary condition by placing a 4-atom Pd cluster upon the 75-atom intact monolayer $VSe_2$ (V: 25 and S: 50) for the $VSe_2$@Pd and a 4-atom Pd cluster upon the 75-atom O-doped monolayer $VSe_2$ (V: 25, O: 3, and S: 47) for $VSe_{2-x}O_x$@Pd. The PAW method was used to describe the wave function of the core region, and the valence wave function was extended to a linear combination of plane waves with 500 eV cutoff energy. The geometry was fully relaxed without any constraint until the force on each atom was less than 0.02 eV/Å. Grimme's DFT-D3 correction was employed for dispersion interaction.

## ASSOCIATED CONTENT

### Supporting Information

The Supporting Information is available free of charge at https://pubs.acs.org/doi/10.1021/jacsau.2c00596.

Supplementary characterizations of the samples, detailed SERS studies of $VSe_{2-x}O_x$@Pd sensor, details of DFT calculations, controlled experiments between the plasmonic Au@Pd NPs and $VSe_{2-x}O_x$@Pd sensor, calculation of the degree of charge-transfer ($\rho_{CT}$), kinetic analysis of the SM reaction (PDF)

## AUTHOR INFORMATION


### Corresponding Authors

**Qi Hao** − *School of Physics, Southeast University, Nanjing 211189, China;* orcid.org/0000-0002-5525-4417; Email: qihao@seu.edu.cn

**Teng Qiu** − *School of Physics, Southeast University, Nanjing 211189, China;* orcid.org/0000-0002-1160-2619; Email: tqiu@seu.edu.cn

### Authors

**Mingze Li** − *School of Physics, Southeast University, Nanjing 211189, China;* orcid.org/0000-0001-8271-5576

**Yunjia Wei** − *School of Physics, Southeast University, Nanjing 211189, China;* orcid.org/0000-0003-3260-0599

**Xingce Fan** − *School of Physics, Southeast University, Nanjing 211189, China;* orcid.org/0000-0002-2508-3063

**Guoqun Li** − *School of Physics, Southeast University, Nanjing 211189, China;* orcid.org/0000-0001-9024-3310

**Xiao Tang** − *School of Physics, Southeast University, Nanjing 211189, China;* orcid.org/0000-0001-9545-247X

**Weiqiao Xia** − *School of Physics, Southeast University, Nanjing 211189, China*

Complete contact information is available at: https://pubs.acs.org/10.1021/jacsau.2c00596


### Author Contributions

‡M.L. and Y.W. contributed equally to this work. The manuscript was written through contributions of all authors. All authors have given approval to the final version of the manuscript. CRediT: **Mingze Li** conceptualization, investigation, methodology, writing-original draft; **Yunjia Wei** conceptualization, investigation, methodology; **Xingce Fan** writing-review & editing; **Guoqun Li** investigation; **Xiao Tang** investigation; **Weiqiao Xia** writing-review & editing; **Qi Hao** funding acquisition, supervision, writing-review & editing; **Teng Qiu** funding acquisition, supervision, writing-review & editing.

### Notes

The authors declare no competing financial interest.

## ACKNOWLEDGMENTS

T.Q. acknowledges the National Natural Science Foundation of China (Grant No. 11874108). Q.H. acknowledges the National Natural Science Foundation of China (Grant No. 22004016).

## REFERENCES


(1) Iqbal, M.; Kaneti, Y. V.; Kim, J.; Yuliarto, B.; Kang, Y.-M.; Bando, Y.; Sugahara, Y.; Yamauchi, Y. Chemical Design of Palladium-Based Nanoarchitectures for Catalytic Applications. *Small* **2019**, *15* (6), 1804378.

(2) Molnar, A. Efficient, Selective, and Recyclable Palladium Catalysts in Carbon- Carbon Coupling Reactions. *Chem. Rev.* **2011**, *111* (3), 2251−2320.

(3) Li, J.; Yang, S.; Wu, W.; Jiang, H. Recent Advances in Pd-Catalyzed Cross-Coupling Reaction in Ionic Liquids. *Eur. J. Org. Chem.* **2018**, *2018* (11), 1284−1306.

(4) Ruiz-Castillo, P.; Buchwald, S. L. Applications of Palladium-Catalyzed C−N Cross-Coupling Reactions. *Chem. Rev.* **2016**, *116* (19), 12564−12649.

(5) Langer, J.; Jimenez de Aberasturi, D.; Aizpurua, J.; Alvarez-Puebla, R. A.; Auguié, B.; Baumberg, J. J.; Bazan, G. C.; Bell, S. E.;

Boisen, A.; Brolo, A. G. Present and Future of Surface-Enhanced Raman Scattering. *ACS Nano* **2020**, *14* (1), 28−117.
(6) Wang, X.; Huang, S.-C.; Hu, S.; Yan, S.; Ren, B. Fundamental Understanding and Applications of Plasmon-Enhanced Raman Spectroscopy. *Nat. Rev. Phys.* **2020**, *2* (5), 253−271.
(7) Baumberg, J. J.; Aizpurua, J.; Mikkelsen, M. H.; Smith, D. R. Extreme Nanophotonics from Ultrathin Metallic Gaps. *Nat. Mater.* **2019**, *18* (7), 668−678.
(8) Zhang, Y.-J.; Radjenovic, P. M.; Zhou, X.-S.; Zhang, H.; Yao, J.-L.; Li, J.-F. Plasmonic Core−Shell Nanomaterials and Their Applications in Spectroscopies. *Adv. Mater.* **2021**, *33* (50), 2005900.
(9) Zhang, H.; Duan, S.; Radjenovic, P. M.; Tian, Z.-Q.; Li, J.-F. Core−Shell Nanostructure-Enhanced Raman Spectroscopy for Surface Catalysis. *Acc. Chem. Res.* **2020**, *53* (4), 729−739.
(10) Linic, S.; Aslam, U.; Boerigter, C.; Morabito, M. Photochemical Transformations on Plasmonic Metal Nanoparticles. *Nat. Mater.* **2015**, *14* (6), 567−576.
(11) Ahmed, I.; Shi, L.; Pasanen, H.; Vivo, P.; Maity, P.; Hatamvand, M.; Zhan, Y. There Is Plenty of Room at the Top: Generation of Hot Charge Carriers and Their Applications in Perovskite and Other Semiconductor-Based Optoelectronic Devices. *Light Sci. Appl.* **2021**, *10* (1), 174.
(12) Wu, K.; Chen, J.; Mcbride, J. R.; Lian, T. Efficient Hot-Electron Transfer by a Plasmon-Induced Interfacial Charge-Transfer Transition. *Science* **2015**, *349* (6248), 632−635.
(13) Lombardi, J. R.; Birke, R. L. A Unified View of Surface-Enhanced Raman Scattering. *Acc. Chem. Res.* **2009**, *42* (6), 734−742.
(14) Lan, L.; Gao, Y.; Fan, X.; Li, M.; Hao, Q.; Qiu, T. The Origin of Ultrasensitive SERS Sensing beyond Plasmonics. *Front. Phys.* **2021**, *16* (4), 43300.
(15) Chen, M.; Liu, D.; Du, X.; Lo, K. H.; Wang, S.; Zhou, B.; Pan, H. 2D Materials: Excellent Substrates for Surface-Enhanced Raman Scattering (SERS) in Chemical Sensing and Biosensing. *TrAC Trends Anal. Chem.* **2020**, *130*, 115983.
(16) Cong, S.; Liu, X.; Jiang, Y.; Zhang, W.; Zhao, Z. Surface Enhanced Raman Scattering Revealed by Interfacial Charge-Transfer Transitions. *Innovation* **2020**, *1* (3), 100051.
(17) Du, X.; Liu, D.; An, K.; Jiang, S.; Wei, Z.; Wang, S.; Ip, W. F.; Pan, H. Advances in Oxide Semiconductors for Surface Enhanced Raman Scattering. *Appl. Mater. Today* **2022**, *29*, 101563.
(18) Li, M.; Wei, Y.; Fan, X.; Li, G.; Hao, Q.; Qiu, T. Mixed-Dimensional van Der Waals Heterojunction-Enhanced Raman Scattering. *Nano Res.* **2022**, *15* (1), 637−643.
(19) Li, M.; Fan, X.; Gao, Y.; Qiu, T. $W_{18}O_{49}$/Monolayer $MoS_2$ Heterojunction-Enhanced Raman Scattering. *J. Phys. Chem. Lett.* **2019**, *10* (14), 4038−4044.
(20) Seo, J.; Lee, J.; Kim, Y.; Koo, D.; Lee, G.; Park, H. Ultrasensitive Plasmon-Free Surface-Enhanced Raman Spectroscopy with Femtomolar Detection Limit from 2D van Der Waals Heterostructure. *Nano Lett.* **2020**, *20* (3), 1620−1630.
(21) Fan, X.; Wei, P.; Li, G.; Li, M.; Lan, L.; Hao, Q.; Qiu, T. Manipulating Hot-Electron Injection in Metal Oxide Heterojunction Array for Ultrasensitive Surface-Enhanced Raman Scattering. *ACS Appl. Mater. Interfaces* **2021**, *13* (43), 51618−51627.
(22) Lan, L.; Yao, H.; Li, G.; Fan, X.; Li, M.; Qiu, T. Structural Engineering of Transition-Metal Nitrides for Surface-Enhanced Raman Scattering Chips. *Nano Res.* **2022**, *15* (4), 3794−3803.
(23) Cong, S.; Yuan, Y.; Chen, Z.; Hou, J.; Yang, M.; Su, Y.; Zhang, Y.; Li, L.; Li, Q.; Geng, F. Noble Metal-Comparable SERS Enhancement from Semiconducting Metal Oxides by Making Oxygen Vacancies. *Nat. Commun.* **2015**, *6*, 7800.
(24) Hou, X.; Fan, X.; Wei, P.; Qiu, T. Planar Transition Metal Oxides SERS Chips: A General Strategy. *J. Mater. Chem. C* **2019**, *7* (36), 11134−11141.
(25) Fan, X.; Li, M.; Hao, Q.; Zhu, M.; Hou, X.; Huang, H.; Ma, L.; Schmidt, O. G.; Qiu, T. High SERS Sensitivity Enabled by Synergistically Enhanced Photoinduced Charge Transfer in Amorphous Nonstoichiometric Semiconducting Films. *Adv. Mater. Interfaces* **2019**, *6* (19), 1901133.
(26) Hou, X.; Zhang, X.; Ma, Q.; Tang, X.; Hao, Q.; Cheng, Y.; Qiu, T. Alloy Engineering in Few-Layer Manganese Phosphorus Trichalcogenides for Surface-Enhanced Raman Scattering. *Adv. Funct. Mater.* **2020**, *30* (12), 1910171.
(27) Li, M.; Gao, Y.; Fan, X.; Wei, Y.; Hao, Q.; Qiu, T. Origin of Layer-Dependent SERS Tunability in 2D Transition Metal Dichalcogenides. *Nanoscale Horiz.* **2021**, *6* (2), 186−191.
(28) Zheng, Z.; Cong, S.; Gong, W.; Xuan, J.; Li, G.; Lu, W.; Geng, F.; Zhao, Z. Semiconductor SERS Enhancement Enabled by Oxygen Incorporation. *Nat. Commun.* **2017**, *8* (1), 1993.
(29) Li, M.; Zhang, T.; Gao, L.; Wei, Y.; Fan, X.; He, Y.; Niu, X.; Wang, J.; Qiu, T. Monitoring Substrate-Induced Electron−Phonon Coupling at Interfaces of 2D Organic/Inorganic van Der Waals Heterostructures with in Situ Raman Spectroscopy. *Appl. Phys. Lett.* **2022**, *120* (18), 181602.
(30) Shi, Y.; Ma, Z.-R.; Xiao, Y.-Y.; Yin, Y.-C.; Huang, W.-M.; Huang, Z.-C.; Zheng, Y.-Z.; Mu, F.-Y.; Huang, R.; Shi, G.-Y. Electronic Metal−Support Interaction Modulates Single-Atom Platinum Catalysis for Hydrogen Evolution Reaction. *Nat. Commun.* **2021**, *12* (1), 3021.
(31) Yang, J.; Li, W.; Wang, D.; Li, Y. Electronic Metal−Support Interaction of Single-Atom Catalysts and Applications in Electrocatalysis. *Adv. Mater.* **2020**, *32* (49), 2003300.
(32) Yu, W.; Li, J.; Herng, T. S.; Wang, Z.; Zhao, X.; Chi, X.; Fu, W.; Abdelwahab, I.; Zhou, J.; Dan, J. Chemically Exfoliated $VSe_2$ Monolayers with Room-Temperature Ferromagnetism. *Adv. Mater.* **2019**, *31* (40), 1903779.
(33) Yang, C.; Feng, J.; Lv, F.; Zhou, J.; Lin, C.; Wang, K.; Zhang, Y.; Yang, Y.; Wang, W.; Li, J. Metallic Graphene-like $VSe_2$ Ultrathin Nanosheets: Superior Potassium-Ion Storage and Their Working Mechanism. *Adv. Mater.* **2018**, *30* (27), 1800036.
(34) Ci, W.; Yang, H.; Xue, W.; Yang, R.; Lv, B.; Wang, P.; Li, R.-W.; Xu, X.-H. Thickness-Dependent and Strain-Tunable Magnetism in Two-Dimensional van Der Waals $VSe_2$. *Nano Res.* **2022**, *15*, 7597−7603.
(35) Brun, M.; Berthet, A.; Bertolini, J. C. XPS, AES and Auger Parameter of Pd and PdO. *J. Electron Spectrosc. Relat. Phenom.* **1999**, *104* (1−3), 55−60.
(36) Li, Z.; Wei, W.; Li, H.; Li, S.; Leng, L.; Zhang, M.; Horton, J. H.; Wang, D.; Sun, W.; Guo, C. Low-Temperature Synthesis of Single Palladium Atoms Supported on Defective Hexagonal Boron Nitride Nanosheet for Chemoselective Hydrogenation of Cinnamaldehyde. *ACS Nano* **2021**, *15* (6), 10175−10184.
(37) Fan, Y.; Zhuo, Y.; Li, L. $SeO_2$ Adsorption on CaO Surface: DFT and Experimental Study on the Adsorption of Multiple $SeO_2$ Molecules. *Appl. Surf. Sci.* **2017**, *420*, 465−471.
(38) Rout, C. S.; Kim, B.-H.; Xu, X.; Yang, J.; Jeong, H. Y.; Odkhuu, D.; Park, N.; Cho, J.; Shin, H. S. Synthesis and Characterization of Patronite Form of Vanadium Sulfide on Graphitic Layer. *J. Am. Chem. Soc.* **2013**, *135* (23), 8720−8725.
(39) Zhang, Z.; Niu, J.; Yang, P.; Gong, Y.; Ji, Q.; Shi, J.; Fang, Q.; Jiang, S.; Li, H.; Zhou, X. Van Der Waals Epitaxial Growth of 2D Metallic Vanadium Diselenide Single Crystals and Their Extra-High Electrical Conductivity. *Adv. Mater.* **2017**, *29* (37), 1702359.
(40) Baylet, A.; Marecot, P.; Duprez, D.; Castellazzi, P.; Groppi, G.; Forzatti, P. In Situ Raman and in Situ XRD Analysis of PdO Reduction and Pd Oxidation Supported on $\gamma$-$Al_2O_3$ Catalyst under Different Atmospheres. *Phys. Chem. Chem. Phys.* **2011**, *13* (10), 4607−4613.
(41) Li, Y.; Hu, Y.; Shi, F.; Li, H.; Xie, W.; Chen, J. C- H Arylation on Nickel Nanoparticles Monitored by in Situ Surface-Enhanced Raman Spectroscopy. *Angew. Chem., Int. Ed.* **2019**, *58* (27), 9049−9053.
(42) Pein, B. C.; Seong, N.-H.; Dlott, D. D. Vibrational Energy Relaxation of Liquid Aryl-Halides X-$C_6H_5$ (X= F, Cl, Br, I). *J. Phys. Chem. A* **2010**, *114* (39), 10500−10507.
(43) Gaikwad, A. V.; Rothenberg, G. In-situ UV-visible study of Pd nanocluster formation in solution. *Phys. Chem. Chem. Phys.* **2006**, *8* (31), 3669−3675.


https://doi.org/10.1021/jacsau.2c00596
*JACS Au* 2023, 3, 468−475

(44) Lombardi, J. R.; Birke, R. L. A Unified Approach to Surface-Enhanced Raman Spectroscopy. *J. Phys. Chem. C* **2008**, *112* (14), 5605−5617.
(45) Song, X.; Wang, Y.; Zhao, F.; Li, Q.; Ta, H. Q.; Rümmeli, M. H.; Tully, C. G.; Li, Z.; Yin, W.-J.; Yang, L. Plasmon-Free Surface-Enhanced Raman Spectroscopy Using Metallic 2D Materials. *ACS Nano* **2019**, *13* (7), 8312−8319.
(46) Tao, L.; Chen, K.; Chen, Z.; Cong, C.; Qiu, C.; Chen, J.; Wang, X.; Chen, H.; Yu, T.; Xie, W. 1T′ Transition Metal Telluride Atomic Layers for Plasmon-Free SERS at Femtomolar Levels. *J. Am. Chem. Soc.* **2018**, *140* (28), 8696−8704.
(47) Ge, Y.; Wang, F.; Yang, Y.; Xu, Y.; Ye, Y.; Cai, Y.; Zhang, Q.; Cai, S.; Jiang, D.; Liu, X. Atomically Thin $TaSe_2$ Film as a High-Performance Substrate for Surface-Enhanced Raman Scattering. *Small* **2022**, *18* (15), 2107027.
(48) Martin, R.; Buchwald, S. L. Palladium-Catalyzed Suzuki-Miyaura Cross-Coupling Reactions Employing Dialkylbiaryl Phosphine Ligands. *Acc. Chem. Res.* **2008**, *41* (11), 1461−1473.
(49) Lennox, A. J.; Lloyd-Jones, G. C. Selection of Boron Reagents for Suzuki−Miyaura Coupling. *Chem. Soc. Rev.* **2014**, *43* (1), 412−443.
(50) Chen, Z.; Vorobyeva, E.; Mitchell, S.; Fako, E.; Ortuño, M. A.; López, N.; Collins, S. M.; Midgley, P. A.; Richard, S.; Vilé, G. A Heterogeneous Single-Atom Palladium Catalyst Surpassing Homogeneous Systems for Suzuki Coupling. *Nat. Nanotechnol.* **2018**, *13* (8), 702−707.
(51) Feng, H.-S.; Dong, F.; Su, H.-S.; Sartin, M. M.; Ren, B. In Situ Investigation of Hot-Electron-Induced Suzuki- Miyaura Reaction by Surface-Enhanced Raman Spectroscopy. *J. Appl. Phys.* **2020**, *128* (17), 173105.
(52) Heo, J.; Ahn, H.; Won, J.; Son, J. G.; Shon, H. K.; Lee, T. G.; Han, S. W.; Baik, M.-H. Electro-Inductive Effect: Electrodes as Functional Groups with Tunable Electronic Properties. *Science* **2020**, *370* (6513), 214−219.
(53) Jiang, P.; Dong, Y.; Yang, L.; Zhao, Y.; Xie, W. Hot Electron-Induced Carbon−Halogen Bond Cleavage Monitored by in Situ Surface-Enhanced Raman Spectroscopy. *J. Phys. Chem. C* **2019**, *123* (27), 16741−16746.
(54) Zhang, C.; Li, Y.; Zhu, A.; Yang, L.; Du, X.; Hu, Y.; Yang, X.; Zhang, F.; Xie, W. In Situ Monitoring of Suzuki-Miyaura Cross-Coupling Reaction by Using Surface-Enhanced Raman Spectroscopy on a Bifunctional Au-Pd Nanocoronal Film. *Chin. Chem. Lett.* **2022**, DOI: 10.1016/j.cclet.2022.06.078.
(55) Wei, Y.; Hao, Q.; Fan, X.; Li, M.; Yao, L.; Li, G.; Zhao, X.; Huang, H.; Qiu, T. Investigation of the Plasmon-Activated C−C Coupling Reactions by Liquid-State SERS Measurement. *ACS Appl. Mater. Interfaces* **2022**, *14*, 54320−54327.


https://doi.org/10.1021/jacsau.2c00596
*JACS Au* 2023, 3, 468−475